Moisture Transport and Water Vapor Budget over the Sahara Desert

Li Zhuo[1] and Liming Zhou*[1]

[1]*Department of Atmospheric and Environmental Sciences, University at Albany, State University of New York, Albany, NY 12222, USA*

*Correspondence:

Liming Zhou

Department of Atmospheric and Environmental Sciences

University at Albany, State University of New York

1400 Washington Avenue, Albany, NY 12222

Tel: (518) 442-4446; Fax: (518) 442-5825

Email: lzhou@albany.edu

Received: 31 December 2021

Revised: 6 March 2022

Accepted: 15 March 2022

First published: 18 March 2022

Key words: Sahara Desert; Moisture transport; Water vapor budget

This work is funded by the National Science Foundation (NSF) AGS-1952745.

ABSTRACT

Previous studies documented that near surface temperatures over the Sahara and Arabian deserts have been amplified in a warming climate, which is termed desert amplification (DA). DA has been linked possibly to the large-scale greenhouse effects associated with increasing water vapor. With very limited moisture availability over the driest desert, two key questions unanswered are the desert moisture sources and the relative contributions of thermodynamic and dynamic processes to the changes in moisture transport. In this study, the atmospheric water vapor budget over the Sahara Desert from 1981-2020 is analyzed to address these two questions. Results indicate that the water vapor content over the Sahara Desert has increased significantly since 1981, primarily during the boreal summer and in the lower to middle troposphere. The water vapor budget analysis indicates that in the boreal summer, most of the added moisture is transported into the Sahara Desert through the intensifying northerly inflow across the northern boundary of the desert, while the other boundaries are all export channels. The northerly inward moisture transport is associated with the ridge in the lower troposphere and the Saharan high above the lower troposphere. Further analysis indicates that both dynamic and thermodynamic factors contribute to the increase of the inward moisture flux at the northern boundary, while the associated interannual variability is dominated by the dynamic component related to the circulation pattern changes. The changes of the circulation pattern in the lower troposphere are manifested as the westward extension of the low over the Arabian Peninsula and as the strengthening of the Saharan high above the lower troposphere, both contributing to the increase of the northerly inward moisture transport.

1. Introduction

The Sahara and Arabian deserts, the largest and driest deserts on Earth, have been argued to have experienced the largest warming rate in the low and middle latitudes (termed desert amplification or DA) based on global-scale analyses of observational, reanalysis and climate model datasets (Zhou et al., 2015; Zhou, 2016; Wei et al., 2017). Similar views were also documented by regional-scale studies (Evan et al., 2015; Cook and Vizy, 2015; Vizy and Cook, 2017; Cook et al., 2021). For example, based on observational and reanalysis datasets, Cook and Vizy (2015) reported that the warming rate of the surface temperature on the Sahara Desert is much larger than that in the tropical regions. The Sahara Desert is also found to have expanded significantly in the past century (Thomas and Nigam, 2018), which is consistent with the concept of DA. The magnitude of DA is found to be strongest near the surface and decreases gradually with height (Wei et al., 2017; Zhou, 2021).

Research on the potential mechanisms driving the DA is still in the early stages (Thomas and Nigam, 2018; Zhou, 2021). Recent studies have attributed the DA likely to the enhanced downward longwave radiation induced by the increasing amounts of greenhouse gases (Evan et al., 2015; Cook and Vizy, 2015; Vizy and Cook, 2017; Zhou, 2016, 2021; Zhou et al., 2016, 2021). Among the greenhouse gases, water vapor is found to play a big role in enhancing the downward longwave radiation over the deserts in response to a warmer and moister atmosphere. For instance, based on the observational and reanalysis datasets, Zhou et al. (2016) documented a negative logarithmic relationship between the total content of water vapor in the atmospheric column and the ratio of downward longwave radiation trend to the total water vapor content trend, indicating the largest efficiency in the greenhouse effect over the driest regions like the Sahara Desert. Using a heat and water vapor budget analysis, Evan et al. (2015) also attributed the increase of the temperature over the Sahara Desert to the enhanced

69 greenhouse warming by moisture. By separating the DA into dry and wet seasons, Vizy and
70 Cook (2017) found that during the wet season, it is the increased amounts of moisture over the
71 Sahara Desert that drives the fast warming of the near surface temperature.

72 The aforementioned studies, however, do not completely address one key question
73 regarding the remote moisture transport and its variability over the Sahara Desert where the
74 local moisture availability is very limited. Vizy and Cook (2017) qualitatively analyzed the
75 changes in circulation patterns over the Sahara Desert and found increased moisture transport
76 into the Sahara Desert via the strengthening of the Sahara low/Saharan high system (Figure 11
77 in their paper). However, a detailed quantitative analysis is still needed to examine the water
78 vapor transport over the Sahara Desert, because there may be multiple mechanisms through
79 which the moisture can be transported into the atmosphere over the desert. For example, it is
80 long established that the African monsoon plays a significant role in the rainfall in the Sahel
81 (Druyan, 2011; Monerie et al, 2016; Odoulami and Akinsanola, 2018; Akinsanola and Zhou,
82 2019a, 2019b) and the southern Sahara (Thomas and Nigam, 2018; Pausata et al., 2020). So
83 the possibility that variations in the African monsoon may also have modified the moisture
84 transported to the Sahara Desert cannot be ruled out. In addition, the change of the moisture
85 content over a specific region could be driven by the dynamic or thermodynamic factors
86 (Seager et al., 2010; Wang et al., 2017; Akinsanola and Zhou, 2019a, 2019b). Separating the
87 dynamic and thermodynamic contributions to the increase of the Sahara Desert moisture also
88 needs in-depth quantitative analysis.

89 Aiming at addressing the questions mentioned above and shedding some light on our
90 understanding of the DA, here we conduct the water vapor budget analysis to analyze the
91 moisture variability over the Sahara Desert. To our best knowledge, no such work has been

done before. The paper is organized as follows. In section 2 we will discuss the data and methods used. The main results and discussion will be given in Section 3. Section 3.1 provides an overview of the moisture trends over the Sahara Desert. Section 3.2 analyzes the results of the water vapor budget. Section 3.3 quantifies the relative contributions of the dynamic and thermodynamic processes to the inward moisture flux. Concluding remarks follow in section 4.

2. Data and Methods

In this paper, we define the Sahara Desert as the region located between 20°N to 30°N and 10°W to 30°E, following previous studies (Harada et al., 2003; Cook and Vizy, 2015). We use two reanalysis datasets, including the fifth major global reanalysis produced by European Centre for Medium-Range Weather Forecasts (ERA5; Hersbach et al., 2020) and the Modern-Era Retrospective Analysis for Research and Applications, version 2 (MERRA-2; Gelaro et al., 2017), for the period 1981-2020. To calculate the moisture budget components, here we use 6-hourly fields of specific humidity (q), zonal and meridional winds (u, v) from ERA5 and MERRA-2 at a horizontal resolution of $1° \times 1°$ and $0.5° \times 0.625°$, respectively. We have also utilized the ERA5 data at the resolution of $0.25° \times 0.25°$ and find that the results are similar. Monthly means quantities, such as horizontal winds, specific humidity and other calculated variables like moisture flux ($\rho q \vec{V}$), and geopotential heights, are aggregated to create the corresponding seasonal and annual mean variables. Here we classify June-August (JJA) as the boreal summer and December-February (DJF) as the boreal winter. The linear trend is calculated via least squares fitting and a two-tailed student's t test is used to test the significance of the trend.

Following previous studies (Sun and Wang, 2014; Wang et al., 2015; Dai et al., 2020;

Mayer et al., 2021), the water vapor budget equation can be written as:

$$\frac{1}{g}\frac{\partial}{\partial t}\int_{p_t}^{p_s} q dp = -\frac{1}{g}\int_{p_t}^{p_s} \nabla\bullet\left(q\vec{V}\right)dp + E - P + R, \quad (1)$$

where g is the gravitational constant, q and $\vec{V}$ are the specific humidity and the horizontal wind vector, respectively, p_s and p_t are the pressure at the surface and top of the atmosphere, respectively. Here we set p_t=300 hPa. The left term of equation (1) is the time change of the total precipitable water (TPW) in a single atmospheric column. The first term on the right hand of equation (1) is the vertically integrated moisture flux convergence (VIMFC). *E* and *P* are the surface evaporation and precipitation rates, respectively. *R* is the residual term.

Using the 2D divergence theorem (Zangvil et al., 2004; Jin et al., 2011; Lamb et al., 2012; Minallah and Steiner, 2021), VIMFC can be written as:

$$\text{VIMFC}=-\frac{1}{g}\int_{p_t}^{p_s} \nabla\bullet\left(q\vec{V}\right)dp = -\frac{1}{Ag}\iint qV_n dl dp, \quad (2)$$

where *dl* is the length of the grid along the latitude and longitude, V_n is the wind vector projected to the normal direction of each boundary, A is the area of the integration region. The right-hand term of equation (2) can be expressed in the form of the total net moisture fluxes across the four boundaries of the Sahara Desert:

$$-\frac{1}{Ag}\iint qV_n dl dp = \frac{1}{A}(-\text{north flux} + \text{south flux} - \text{east flux} + \text{west flux}), \quad (3)$$

where the right-hand terms of equation (3) represent the moisture flux across the northern, southern, eastern and western boundaries, respectively. For convenience, here we rewrite equation (3) as:

$$-\frac{1}{Ag}\iint qV_n dl dp = \mathrm{F_{north}} + \mathrm{F_{south}} + \mathrm{F_{east}} + \mathrm{F_{west}}, \quad (4)$$

where $\mathrm{F_{north}}$, $\mathrm{F_{south}}$, $\mathrm{F_{east}}$ and $\mathrm{F_{west}}$ represent the moisture transport across the northern, southern, eastern and western boundaries, respectively.

To further quantify the relative contributions of thermodynamic and dynamic processes to

the change of the moisture transports, here we decompose the moisture flux across a certain boundary into anomalies due to changes of wind and specific humidity respectively, following previous studies (Wang et al., 2017; Seager et al., 2010; Akinsanola and Zhou, 2019):

$$\frac{1}{g}\iint -qV_n dldp = \frac{1}{g}\iint -\bar{q}\bar{V}_n dldp + \frac{1}{g}\iint -q'\bar{V}_n dldp + \frac{1}{g}\iint -\bar{q}V_n' dldp + \frac{1}{g}\iint -q'V_n' dldp, \quad (5)$$

where $\bar{V}_n$ and $\bar{q}$ are the 40-year (1981-2020) climatology of the wind normal to a specific boundary and specific humidity in a specific season or year, and V_n' and q' are the respective deviations from the 40-year climatology of each year or season. The term on the left-hand of equation (5) is the moisture flux across a certain boundary. The first term on the right hand of equation (5) is the average term, which is constant within 40 years. The second term and third term are the moisture flux anomalies caused by the thermodynamical (thermodynamic term) and dynamical processes (dynamic term), respectively. The last term can be neglected for both q' and V_n' are small deviations from the climatology (Wang et al., 2017).

3. Results and discussion

3.1 Moisture trends in ERA5 and MERRA-2

Figure 1 displays the spatial distribution of JJA, DJF and annual TPW climatology in ERA5 (left) and MERRA-2 (right). The comparison between the left and right columns highlights the great similarity in TPW between the two reanalysis datasets over the Sahara Desert, especially for JJA and annual TPW. The differences in DJF TPW are relatively larger than the differences in JJA and annual TPW. However, as shown later, the moistening over the Sahara Desert mainly takes place in JJA and such differences in DJF will not matter much in our study.

The spatial patterns of JJA, DJF and annual TPW trends in ERA5 and MERRA-2 are

160 shown in Figure 2. Comparing the left columns to the right columns, one can see that the two
161 datasets display similar moistening trends in both the spatial patterns and magnitude. In JJA,
162 both indicate positive TPW trends that are statistically significant at the 99% confidence level
163 over most areas in the Sahel and the Sahara Desert (depicted as the rectangle box in blue), with
164 the maximum of the magnitude located in the Sahel (Figure 2a, b). There is evidence of a
165 significant moistening trend around the west coastline of the African land at 16°N in MERRA-
166 2 (Figure 2b), which is absent in ERA5 (Figure 2a). However, this difference is out of the area
167 of our study domain and thus will not influence our further analysis over the Sahara Desert. In
168 DJF, neither ERA5 or MERRA-2 exhibits statistically significant moistening trends over the
169 Sahara Desert (Figure 2c-d). The annual trends of TPW in ERA5 also correspond well to the
170 trends in MERRA-2 in terms of the spatial patterns and magnitude, as both exhibit positive
171 TPW trends over the Sahara Desert and the Sahel (Figure 2e-f). It is noteworthy that the spatial
172 patterns of the annual TPW trends share great similarity with the JJA TPW trends in both ERA5
173 and MERRA-2 (Figure 2a-b; e-f). Such similarity indicates that the moistening over the Sahara
174 Desert mainly takes place in JJA, which is in agreement with Vizy and Cook (2017). We have
175 also examined the trends of TPW in boreal spring and autumn and find that TPW shows no
176 significant changes in the boreal spring, while in the boreal autumn TPW displays relatively
177 weaker positive trends over parts of the Sahara Desert (figures now shown). Overall, the
178 consistency in two datasets illustrates that the Sahara Desert has been indeed experiencing a
179 significant moistening in JJA since 1981 and bolsters our confidence in further analysis.
180 Since the increase of TPW mainly occurs in JJA, our subsequent analysis will focus only
181 on the boreal summer. Figure 3 shows the water vapor content trends at different layers from
182 two datasets. Similar to TPW, ERA5 and MERRA-2 are overall in good agreement with each

other in terms of the moisture content trends at different layers over the Sahara Desert. In the lower troposphere below 900 hPa (Figure 3a-b), the trends of moisture content in ERA5 and MERRA-2 are positive and statistically significant over most areas of the Sahara Desert, even though the strongest moistening takes place south in the location of the monsoon trough (Thorncroft et al., 2011; Cook and Vizy, 2015; Vizy and Cook, 2017). The water vapor content between 900 and 700 hPa also displays statistically significant positive trends over the Sahara Desert, with the associated magnitude even larger than that in the lower troposphere below 900 hPa (Figure 3a-d). For the layer between 700 and 500 hPa, the trends of the water vapor content over the Sahara are still overall positive and statistically significant (Figure 3e-f). This suggests that the increase of moisture over the Sahara Desert in JJA is not confined to the lower troposphere but extends to the middle troposphere. In addition, the mechanism responsible for the moistening in the lower troposphere may differ from that in the middle troposphere.

To further quantitatively assess the vertical profile of the moistening rates over the Sahara Desert, here we calculate the area average q trends at different pressure levels over the Sahara Desert in JJA from the two reanalysis datasets (Figure 4). One can see that the vertical profile of the area average q trend over the Sahara Desert in ERA5 is similar to that in MERRA-2 to some extent. Moistening statistically significant at the 99% confidence level extends upwards to 400 hPa in ERA5 and 500 hPa in MERRA-2. This further testifies that the increase of water vapor content over the Sahara Desert in JJA occurs from the lower to middle troposphere.

3.2 Water vapor budget analysis for the Sahara Desert

To quantify the contributions of different physical processes to the moistening of the atmosphere over the Sahara Desert in JJA, in this section we will conduct the water vapor budget analysis for the atmosphere over the desert. By combining with equations (2) and (4),

206 equation (1) can be written as:

207 $$\frac{1}{g}\frac{\partial}{\partial t}\int_{p_t}^{p_s} q dp = \mathrm{F}_{\mathrm{north}} + \mathrm{F}_{\mathrm{south}} + \mathrm{F}_{\mathrm{east}} + \mathrm{F}_{\mathrm{west}} + E - P + R, \quad (6)$$

208 The results of the water vapor budget and the trends of each term are listed in table 1.
209 ERA5 and MERRA-2 generally agree well with each other in both the values and trends of
210 each term. Table 1 highlights that the moisture transport across the northern boundary
211 dominates the contribution to the increase of the moisture content, as the values and trends of
212 $\mathrm{F}_{\mathrm{north}}$ are largest in both ERA5 and MERRA-2. While the northern boundary is the import
213 channel, other boundaries are all the export channels, with only the eastern boundaries display
214 a statistically significant trend. It is noteworthy that the moisture transport across each
215 boundary is all of an order magnitude larger than the evaporation, precipitation and residual
216 terms, which is expected as the evaporation and precipitation are rather small over the hot dry
217 desert (Figure S1). Even though the evaporation and precipitation show statistically significant
218 trends, the trends are much smaller than those of the moisture transport across the four
219 boundaries. It is noteworthy that evaporation displays trends with different significance levels
220 in the two reanalysis datasets, possibly due to the different soil moisture in ERA5 and MERRA-
221 2. Exploring the relationship between the difference in soil moisture and evaporation is beyond
222 the scope of this paper and will be a potential subject of future studies. Since it is the moisture
223 transport across the four boundaries that dominate the moisture variability over the Sahara
224 Desert, we will focus on the water vapor transport next.

225 *3.2.1 Climatological moisture transport in JJA*

226 Figure 5 shows the moisture transport and geopotential height climatology in JJA over the
227 Sahara Desert for ERA5. We have examined the climatology in MERRA-2 as well and the
228 results are similar (figures not shown). In the lower troposphere in JJA, the northern African

land is characterized by a monsoon trough centered around the Sahel (Figure 5a). The trough is converged by the northward moisture advection associated with the African monsoon to the south and the southward moisture transport accompanying the weak ridge across the Mediterranean Sea. The induced water vapor convergence can well explain the strong moistening in the Sahel (Figure 2a-b; Figure 3). This climatological circulation pattern is consistent with previous studies (Neupane and Cook, 2013; Vizy et al., 2013; Cook and Vizy, 2015; Thorncroft et al., 2015).

Figure 5a highlights two branches of inward moisture transport into the Sahara Desert in the lower troposphere in JJA. One is the northerly moisture transport brought by the weak ridge across the Mediterranean Sea, another branch is the southerly moisture transport related to the African monsoon. However, the northward African monsoon seems to be only able to reach around 18°N (Figure 5a), which agrees well with previous work (Lélé and Leslie, 2016). Even though the climatology may mask some extreme cases, this climatological circulation pattern implies to some extent that the contribution from the African monsoon to the increase of moisture content over the Sahara Desert in JJA may be small, though it indeed plays an important role in the Sahelian rainfall (Akinsanola and Zhou, 2019a, 2019b).

The circulation pattern mentioned above, with a monsoon trough to the south and a weak ridge to the north, extends upwards to around 850 hPa, as the weak cyclonic circulation can also be detected south of 20°N while the weak ridge to the north becomes a high with a closed circulation (Figure 5b). Above 850 hPa, the circulation climatology over the northern African land is characterized by an overwhelming Saharan high (Figure 5b-d). South of the Saharan high is the African easterly jet (Cook, 1999), which strongly intensifies the magnitude of the westward moisture transport over Sahel. The jet can also be detected at much higher levels on

252 500 hPa at the southern boundary of the subtropical high (Figure 5d).

253 Similar to the weak ridge at the lower troposphere (Figure 5a), the Saharan high at higher
254 levels consistently transports the moisture from the Mediterranean Sea southward into the
255 Sahara Desert via the northerly flow (Figure 5b-d). On the contrary, the northward moisture
256 flux related to the African monsoon gradually diminishes with height (Figure 5a-d), which
257 means that the moisture brought in by the monsoon is confined to the lower troposphere. The
258 comparison between these two types of moisture transport suggests that the southward moisture
259 transport associated with the Saharan high in the middle troposphere and weak ridge in the
260 lower troposphere may play a much more important role in the moistening of the atmosphere
261 over the Sahara Desert in JJA than the northward African monsoon does. This is consistent with
262 the results of the water vapor budget, which indicates that the increased moisture mainly comes
263 from the northern boundary while the southern boundary is an export channel (Table 1).

264 In summary, there are two branches of inward flow that transports water vapor into the
265 Sahara Desert in JJA. One is associated with the northward African monsoon at the southern
266 boundary in the lower troposphere, another is related to the ridge (Saharan high) at the northern
267 boundary. The contribution of the former is expected to be much smaller than the latter.

268 *3.2.2 Moisture flux across each boundary*

269 Figure 6 displays the climatology of the integrated water vapor transport (IVT) and the
270 moisture fluxes at each boundary for ERA5 (a) and MERRA-2 (b) in JJA. Here IVT is defined
271 following previous studies on atmospheric rivers (Mundhenk et al., 2016; Kamae et al., 2017;
272 Zavadoff et al., 2020; Zhou et al., 2021):

273 $$\mathrm{IVT} = \frac{1}{g}\int_{p_t}^{p_s} q\vec{V}\,dp, \qquad (7)$$

274 where g, p_s, p_t, $\vec{V}$, q are defined in section 2. The spatial pattern of IVT in ERA5 (Figure 6a)

is similar to that in MERRA-2 (Figure 6b), as both highlights a branch of northerly inward moisture flux associated with the Saharan high at the northern boundary of the Sahara Desert (Figure 5b-d; Figure 6a-b). It is also noteworthy that the signal of the northward African monsoon at lower levels totally disappears in the spatial pattern of IVT south of the Sahara Desert (Figure 5a; Figure 6a-b). This illustrates that the African easterly jet, the direction of which is almost opposite to that of the low-level African monsoon (Figure 5), dominates the moisture flux in JJA over the Sahel.

Following equation (3), here we calculate the moisture flux for each boundary of the Sahara Desert for ERA5 (a) and MERRA-2 (b), the direction and intensity of the moisture fluxes are also shown in Figure 6 (arrows and numbers in red). Again, ERA5 and MERRA-2 exhibit similar moisture flux across the four boundaries in terms of magnitude and direction, except for the western boundary (Figure 6a-b). From Figure 6, one can see that for the Sahara Desert, the incoming moisture channel is at the northern boundary, while the west, south and east boundaries are all export channels, which is consistent with the results of the water vapor budget (Table 1). Obviously, the intensity of the inward moisture fluxes at the northern boundary is an order of magnitude larger than those outward moisture fluxes at other boundaries (Figure 6a-b). This indicates that the southward moisture flux associated with the Saharan high (weak ridge at lower levels) is the main contributor to the increased water vapor content over the Sahara Desert in JJA, and the Mediterranean Sea is one of the most important moisture supply sources for the increasing moisture over the Sahara Desert.

To test the robustness of our results, we have also moved the southern boundaries further southward and found that the results are similar (figures not shown). Another feature of interest is the difference of the moisture flux across the western boundary between ERA5 (Figure 6a)

298 and MERRA-2 (Figure 6b). This difference is related to the different West African westerly jet
299 (WAWJ) in the two reanalysis datasets. As shown in Figure 6b, MERRA-2 displays stronger
300 WAWJ and thus larger moisture flux at the western boundary than ERA5, which can well
301 explain the significant moistening trend around the west coastline of the African land in
302 MERRA-2 (Figure 2b, f). Previous studies indicated that WAWJ plays a key role in the moisture
303 transport and rainfall variability over West Africa during the boreal summer (Pu and Cook,
304 2012; Liu et al., 2020). It is meaningful to explore the differences of WAWJ in the two
305 reanalysis datasets, which, however, is beyond the scope of this paper and will be a subject of
306 future studies.

307 Figure 7 displays the interannual variability of the moisture fluxes across each boundary.
308 The two reanalysis datasets exhibit similar interannual variability and comparable trends of the
309 moisture fluxes except for the western boundary (Figure 7a-d). Figure 7 highlights the
310 statistically significant ($p<0.01$) moisture inflow and outflow transport at the northern and
311 eastern boundary respectively, while the trends of the moisture flux at the southern and western
312 boundaries are statistically insignificant (Figure 7a-b). It is also noteworthy that the magnitudes
313 of the inward moisture flux trends at the northern boundary in both reanalysis datasets are larger
314 than the corresponding magnitudes of the outward moisture flux trend at the eastern boundary
315 (Figure 7a-b). This demonstrates that the moisture content transported inward via the northerly
316 inflow across the northern boundary is increasing at a much faster rate than the moisture content
317 transported outward across the eastern boundary, which is responsible for the moistening of the
318 atmosphere over the Sahara Desert in JJA and consistent with the results of the water vapor
319 budget (Table 1).

320 To further elucidate the relationships between the moisture fluxes with the large-scale

systems, here we study the vertical profiles of the climatological moisture transport (contours) and the associated trends (shadings) at each boundary (Figure 8). Similar to previous analyses, ERA5 and MERRA-2 exhibit similar vertical profile patterns of the climatological moisture transport and the associated trends except for the western boundary, where below 600 hPa the moisture transport trends in MERRA-2 and ERA5 are opposite (Figure 8d, h). However, both the trends in MERRA-2 and ERA5 below 600 hPa at the western boundary are statistically insignificant and thus will not matter that much in our study (Figure 8d, h).

Figure 8a, e highlights that the northern boundary is dominated by the northerly inward moisture fluxes from the prime meridian to 20°E, while the part west of prime meridian is characterized by the southerly outward moisture flux, which is related to the southerly flow of the Saharan high and the ridge (Figure 5). The dominant northerly moisture transport at the northern boundary is associated with the ridge and Saharan high to the north (Figure 5). Of particular importance is that the northerly inward moisture transport at the northern boundary is mostly characterized by a statistically significant negative (intensifying) trend (Figure 8a, e). The negative trend of the northerly moisture transport is characterized by two local maximums, with one in the lower troposphere at about 20°E and another in the middle troposphere (700 hPa) at the prime meridian (Figure 8a, e). This suggests that the northerly inward moisture transport associated with the ridge and the Saharan high above are both intensifying, contributing to the increase of the water vapor content over the Sahara Desert (Figure 5). Another fact of interest is that the maximum of the northerly moisture transport tilts westward with the height (Figure 8a, e), indicating a displacement between the ridge at lower levels and the Saharan high above. The displacement can also be slightly detected in Figure 5, as the closed Saharan high above the lower troposphere is located west of the ridge in the lower

344 troposphere.

345 The vertical profiles of the moisture fluxes at other boundaries are also consistent with the
346 circulation patterns shown in Figure 5. At the southern boundary (Figure 8b, f), one can see the
347 shallow northward moisture transport related to the African monsoon in the lower troposphere,
348 which may contribute some amounts of moisture in the atmosphere over the Sahara Desert.
349 However, such moisture transport is confined to the lower troposphere. Above this shallow
350 northward moisture transport related to the African monsoon, the southern boundary is overall
351 characterized by the northerly moisture flux associated with the Saharan high, which also
352 features an increasing trend in the middle troposphere (Figure 8b, f). As a result, the overall
353 moisture flux across the whole southern boundary is still southward (Figure 6a, b), which
354 further testifies that the contribution of the southerly moisture flux associated with the
355 northward monsoon to the moistening of the atmosphere over the Sahara Desert is relatively
356 small. The eastern boundary is characterized by the increasing outward westerly moisture flux
357 related to the northwest flow circulating the Saharan high (Figure 5b-d), while the prominent
358 feature in the western boundary is the increasing easterly moisture flux related to the easterly
359 jet at about 20°N (Figure 5c-d). The intensifying easterly moisture flux signifies a strengthening
360 African easterly jet, which is consistent with previous studies (Vizy and Cook, 2017).

361 In summary, the water vapor budget analysis demonstrates that most of the added moisture
362 in JJA is transported into the Sahara Desert through the northern boundary via the northerly
363 flow related to the Saharan high and the weak ridge, while the contribution from the African
364 monsoon in the lower troposphere is relatively small. In addition, the northerly inward moisture
365 transport is characterized by a statistically significant increasing trend, which drives the
366 moistening of the atmosphere over the Sahara Desert in JJA.

3.3. Dynamic and thermodynamic contributions to the increase and variability of the inward moisture transport across the northern boundary

As shown in the previous section, the moisture flux across the northern boundary is increasing since 1981, which is the key contributor to the moistening of the atmosphere in JJA over the Sahara Desert. The reason for such increase can be either attributable to the intensification of the wind or the increase of q at the northern boundary. To further investigate which dominates the increase of the inward moisture flux at the northern boundary, here we decompose the moisture flux at the northern boundary into dynamic and thermodynamic terms following equation (5). In addition, the interannual variability of the inward moisture flux is also examined.

The interannual variations in the decomposition of the moisture flux across the northern boundary for ERA5 (a) and MERRA-2 (b) are given in Figure 9. From Figure 9a, b, one can see that dynamic term (blue) exhibits larger variability than the thermodynamic term (red) does. Of particular importance is that the variability of the dynamic term is very close to that of the northern moisture flux (Figure 7a). For ERA5, the correlation coefficient between the dynamic term and the total moisture flux at the northern boundary is 0.91, which is statistically significant ($p<0.0001$). On the contrary, the correlation coefficient between the thermodynamic term and the total moisture flux at the northern boundary is only about -0.2 and not statistically significant. The corresponding correlation coefficients in MERRA-2 is 0.87 ($p<0.0001$) and -0.06 ($p>0.1$), respectively (Figure 9b). This indicates that the interannual variability of the moisture flux at the northern boundary is mainly controlled by the dynamic term. In other words, the changes of the circulation patterns dominate the variability of the inward moisture flux at the northern boundary.

Another consensus between the two datasets highlighted in Figure 9 is that both the thermodynamic and dynamic terms have shown a tendency towards negative since 1981, and the trends of the dynamic terms are larger than those of thermodynamic terms, even though the trend of the dynamic term in MERAA2 is not statistically significant. This indicates that both the dynamic and thermodynamic processes contribute to the increase of the inward moisture transport at the northern boundary. Note that the values of the inward moisture flux at the northern boundary are negative as the inward flux flows from north to south (Figure 7a). The thermodynamic process involves the increase of specific humidity against fixed circulation patterns. Seager et al. (2010) attributes such increase primarily to the water vapor feedback in a warming climate under a fixed relative humidity. Here we examined the specific humidity and relative humidity at 925 hPa and found that the relative humidity at the northern boundary indeed exhibits no significant changes (figure not shown), which is expected considering the large warming associated with the DA and the lack of local moisture availability. The little change in RH and the increase in specific humidity over the desert is primarily a result of moisture advection remotely from surrounding oceans. These results again indicate that the thermodynamic process may be dominated by the large-scale increasing specific humidity in a warming climate associated with the positive water vapor feedback, which is consistent with previous studies (Zhou et al., 2016).

Since the dynamic term also exhibits large contributions to the positive trend of the inward moisture flux at the northern boundary, here the changes of the circulation patterns from 1981 to 2020 over the Sahara Desert in JJA are examined. In the middle troposphere, the positive trends extending from the northeast African land to the Atlantic indicates a westward shift and expansion of the mid-level ridge and an intensifying Saharan high (Figure 10a-d). The

intensification can also be detected via the trends of the moisture transport, with the enhanced northerly wind anomalies in both ERA5 and MERRA-2 in the northwest corner of the African land (Figure 10b, d). The increasing southward inward moisture transport accompanying the strengthening Saharan high at the northern boundary of the African land corresponds well to the midlevel maximum of the positive moisture flux trends in Figure 8a, e, which transports an increasing amount of water vapor into the atmosphere over the Sahara Desert.

To further testify the intensification of the Saharan High, we evaluate the intensity of the Saharan High quantitatively. Following Sun et al. (2017), here the intensity is defined as the maximum 700 hPa geopotential height over the area from 15°N to 40°N and -15°W to 30°E. The interannual variation of the intensity is given in Figure 11. Both ERA5 and MERRA-2 display statistically significant positive trends, indicating that the Saharan High has been strengthening from 1981 to 2020. We also examined the position and size of the Saharan High. The position is defined as the location of the geopotential height maximum. Following Sun et al. (2017), we scale the geopotential height and then choose 38 gpm anomalies to define the extent of the Saharan High (Figure S2). We found that the Saharan High has not moved (figure not shown) but indeed expanded significantly from 1981 to 2020 (Figure S3).

In the lower troposphere, MERRA-2 exhibits positive geopotential height trends south of 20°N and negative trends north of 20°N over the African land, pointing to a northward shift of the monsoon trough over the Sahel (Figure 12c-d), which is in agreement with previous studies (Shekhar and Boos, 2017; Vizy and Cook, 2017). Such a dipole pattern and the shift of the monsoon trough can also be detected in ERA5 (Figure 12a-b). Over the Mediterranean Sea, both ERA5 (Figure 12b) and MERRA-2 (Figure 12d) display statistically significant ($p<0.05$) negative trends of geopotential heights. This is consistent with the results shown in Vizy and

436 Cook (2017) and Skinner et al. (2012). These changes may reflect the westward extension of
437 the low over the Arabian Peninsula (Figure 12a-b), which intensifies the magnitude of the
438 accompanied northerly winds and thus brings more moisture from the Mediterranean Sea into
439 the lower troposphere over the Sahara Desert. The area of the intensifying northerly moisture
440 transport due to the westward extension of the low corresponds well spatially to the negative
441 trends of moisture transport in the lower troposphere shown in Figure 8a, e, which constitutes
442 the water vapor transport channel at lower levels. This suggests that the circulation change over
443 the Arabian Peninsula may impact the Sahara Desert as well.

444 **4. Conclusions**

445 Previous studies suggest that the Sahara Desert is experiencing a fast rate of warming
446 (Zhou et al., 2015; Cook and Vizy, 2015; Zhou, 2016; Wei et al., 2017). Many studies have
447 linked this warming to the enhanced downward longwave radiation associated with increasing
448 amounts of water vapor over the desert (Evan et al., 2015; Zhou et al., 2016; Vizy and Cook,
449 2017). Aiming at answering two questions as to where the increased moisture over the Sahara
450 Desert comes from and how do the thermodynamic and dynamic processes contribute relatively
451 to the changes of the moisture transport, here we use two reanalysis datasets (ERA5 and
452 MERRA-2) to do the moisture budget over the Sahara Desert from 1981 to 2020. We find that
453 the atmosphere over the Sahara Desert has been experiencing a significant moistening since
454 1981, and such increase of moisture mainly takes place in JJA. The moistening is not confined
455 to the lower troposphere, but extends upwards to the middle troposphere.

456 The climatology of the moisture transport shows that in the lower troposphere over the
457 Sahara Desert in JJA, there are two branches of inward water vapor flux, one is associated with
458 the northward African monsoon and the other is related to the weak ridge across the

Mediterranean Sea to the north. In the middle troposphere, the main water vapor channel is the northerly moisture transport related to the Saharan high, while the northward African monsoon is confined to the lower troposphere and is absent in the middle troposphere. The water vapor budget analysis indicates that the northern boundary is the main channel through which the moisture is transported into the Sahara Desert via the northerly inward moisture flux accompanying the weak ridge in the lower troposphere and Saharan high in the middle troposphere, while the other boundaries are the export channels. Additionally, the northerly moisture flux across the northern boundary is increasing at a faster rate than the outward moisture flux at other boundaries, driving the net increase of moisture over the Sahara Desert in JJA.

The decomposition of the northerly moisture flux shows that the interannual variability of the increasing inward moisture flux at the northern boundary is dominated by the dynamic process. However, both dynamic and thermodynamic processes contribute to the increasing trend of the inward water vapor transport at the northern boundary. The thermodynamic process is attributed to the overall large-scale increase of specific humidity in a warming climate associated with the positive water vapor feedback, while the dynamic process is linked to the circulation pattern changes that intensify the northerly moisture flux at the northern boundary. Further trend analysis shows that in the middle troposphere, the increasing northerly moisture transport is associated with the intensifying Saharan high. In the lower troposphere, the increased northerly water vapor transport is linked to the westward extension of the low over the Arabian Peninsula. These two changes all strengthen the northerly winds and thus favor the increase of the inward moisture transport at the northern boundary. This indicates that the Mediterranean Sea may be an important source of moisture for the Sahara Desert.

However, it is still possible that the moisture comes from the Atlantic Ocean, or the Indian Ocean. Further analysis of the origin of the increased moisture over the Sahara Desert needs to trace the path of the water vapor, which involves the use of models and will be a subject of future work. In addition, previous studies have shown that in the boreal summer, there exist some remote influences on the Sahara Desert, such as the Indian monsoon (Rodwell and Hoskins, 1996). Such remote control on the moisture and its transport is not clear and still needs further research. It is also possible that the moisture content change in the middle troposphere over the Sahara Desert may be related to the change of cloud cover over the desert. Given the uncertainty of the cloud cover in the data and models, this relationship still needs further in-depth research. Additionally, significant regional variability in moisture transport may also exist in the Sahara Desert, which will also be the potential subject of future studies.

Acknowledgments. This research is supported by the National Science Foundation (NSF) AGS-1952745. We thank Dr. Samar Minallah for sharing the code on the water vapor budget. Gratitude is also extended to Dr. Edward K. Vizy for the help on calculating the moisture transport trends. We sincerely thank Dr. Brian Rose for the insightful discussions and comments that helped improve the quality of our work.

REFERENCES

Akinsanola, A. A., and Zhou, W., 2019a: Dynamic and thermodynamic factors controlling increasing summer monsoon rainfall over the West African Sahel. Climate Dynamics, 52, 4501–4514. https://doi.org/10.1007/s00382-018-4394-x.

Akinsanola, A. A., and Zhou, W., 2019b: Projections of West African summer monsoon

505 rainfall extremes from two CORDEX models. Climate Dynamics, 52, 2017–2028.
506 https://doi.org/10.1007/s00382-018-4238-8.
507 Cook, K. H., 1999: Generation of the African easterly jet and its role in determining West
508 African precipitation. Journal of Climate, 12, 1165–1184. https://doi.org/10.1175/1520-
509 0442(1999)012<1165:GOTAEJ>2.0.CO;2.
510 Cook, K. H., and Vizy, E. K., 2015: Detection and analysis of an amplified warming of the
511 Sahara Desert. Journal of Climate, 28, 6560–6580. https://doi.org/10.1175/JCLI-D-14-00230.1.
512 Cook, K. H., E. K. Vizy, Y. Liu, and W. Liu, 2021: Greenhouse-gas induced warming
513 amplification over the Arabian Peninsula with implications for Ethiopian rainfall. Climate
514 Dynamics, 57, 3113–3133. https://doi.org/10.1007/s00382-021-05858-x.
515 Dai, L., Wright, J. S., and Fu, R., 2020: Moisture and energy budget perspectives on summer
516 drought in north china. Journal of Climate, 33, 10149–10167. https://doi.org/10.1175/JCLI-D-
517 20-0176.1.
518 Druyan, L. M., 2011: Studies of 21st-century precipitation trends over West Africa.
519 International Journal of Climatology, 31, 1415–1424. https://doi.org/10.1002/joc.2180.
520 Evan, A. T., Flamant, C., Lavaysse, C., Kocha, C., and Saci, A., 2015: Water vapor-forced
521 greenhouse warming over the Sahara Desert and the recent recovery from the Sahelian drought.
522 Journal of Climate, 28, 108–123. https://doi.org/10.1175/JCLI-D-14-00039.1.
523 Gelaro, R., and Coauthors, 2017: The modern-era retrospective analysis for research and
524 applications, version 2 (MERRA-2). Journal of Climate, 30, 5419–5454.
525 https://doi.org/10.1175/JCLI-D-16-0758.1.
526 Harada, C., Sumi, A., and Ohmori, H., 2003: Seasonal and year-to-year variations of rainfall
527 in the Sahara desert region based on TRMM PR data. Geophysical Research Letters, 30, 6–9.

https://doi.org/10.1029/2002GL016695.

Hersbach, H., and Coauthors, 2020: The ERA5 global reanalysis. Quarterly Journal of the Royal Meteorological Society, 146, 1999–2049. https://doi.org/10.1002/qj.3803.

Jin, F., Kitoh, A., and Alpert, P., 2011: Climatological relationships among the moisture budget components and rainfall amounts over the Mediterranean based on a super-high-resolution climate model. Journal of Geophysical Research Atmospheres, 116, 1–13. https://doi.org/10.1029/2010JD014021.

Lamb, P. J., Portis, and D. H., Zangvil, A., 2012: Investigation of large-scale atmospheric moisture budget and land surface interactions over U.S. Southern great plains including for CLASIC (June 2007). Journal of Hydrometeorology, 13, 1719–1738. https://doi.org/10.1175/JHM-D-12-01.1.

Liu, W., Cook, K. H., and Vizy, E. K., 2020: Role of the West African westerly jet in the seasonal and diurnal cycles of precipitation over West Africa. Climate Dynamics, 54, 843–861. https://doi.org/10.1007/s00382-019-05035-1.

Mayer, J., Mayer, M., and Haimberger, L., 2021: Consistency and homogeneity of atmospheric energy, moisture, and mass budgets in ERA5. Journal of Climate, 34, 3955–3974. https://doi.org/10.1175/JCLI-D-20-0676.1.

Minallah, S., and Steiner, A. L., 2021: Role of the atmospheric moisture budget in defining the precipitation seasonality of the great lakes region. Journal of Climate, 34, 643–657. https://doi.org/10.1175/JCLI-D-19-0952.1.

Monerie, P. A., Biasutti, and M., Roucou, P., 2016: On the projected increase of Sahel rainfall during the late rainy season. International Journal of Climatology, 36, 4373–4383. https://doi.org/10.1002/joc.4638.

551 Mundhenk, B. D., Barnes, E. A., Maloney, E. D., and Nardi, K. M., 2016: Modulation of
552 atmospheric rivers near Alaska and the U.S. west coast by Northeast Pacific height anomalies.
553 Journal of Geophysical Research Atmospheres, 121, 12,751-12,765.
554 https://doi.org/10.1002/2016JD025350.
555 Neupane, N., and Cook, K. H., 2013: A nonlinear response of Sahel rainfall to Atlantic
556 warming. Journal of Climate, 26, 7080–7096. https://doi.org/10.1175/JCLI-D-12-00475.1.
557 Odoulami, R. C., and Akinsanola, A. A., 2018: Recent assessment of West African summer
558 monsoon daily rainfall trends. Weather, 73, 283–287. https://doi.org/10.1002/wea.2965.
559 Pausata, F. S. R., Gaetani, M., Messori, G., Berg, A., Maia de Souza, D., Sage, R. F., and
560 deMenocal, P. B., 2020: The Greening of the Sahara: Past Changes and Future Implications.
561 One Earth, 2, 235–250. https://doi.org/10.1016/j.oneear.2020.03.002.
562 Pu, B., and Cook, K. H., 2012: Role of the west African westerly jet in sahel rainfall variations.
563 Journal of Climate, 25, 2880–2896. https://doi.org/10.1175/JCLI-D-11-00394.1.
564 Rodwell, M. J., and Hoskins, B. J., 1996: Monsoons and the dynamics of deserts. Quarterly
565 Journal of the Royal Meteorological Society, 122, 1385–1404.
566 https://doi.org/10.1002/qj.49712253408.
567 Seager, R., Naik, N., Vecchi, and G. A., 2010: Thermodynamic and dynamic mechanisms for
568 large-scale changes in the hydrological cycle in response to global warming. Journal of Climate,
569 23, 4651–4668. https://doi.org/10.1175/2010JCLI3655.1.
570 Shekhar, R., and Boos, W. R., 2017: Weakening and shifting of the Saharan shallow meridional
571 circulation during wet years of the West African monsoon. Journal of Climate, 30, 7399–7422.
572 https://doi.org/10.1175/JCLI-D-16-0696.1.
573 Skinner, C. B., Ashfaq, M., and Diffenbaugh, N. S., 2012: Influence of twenty-first-century

574 atmospheric and sea surface temperature forcing on West African climate. Journal of Climate,
575 25, 527–542. https://doi.org/10.1175/2011JCLI4183.1.
576 Sun, B., and Wang, H., 2014: Moisture sources of semiarid grassland in China using the
577 lagrangian particle model FLEXPART. Journal of Climate, 27, 2457–2474.
578 https://doi.org/10.1175/JCLI-D-13-00517.1.
579 Sun, X., Cook, K. H., and Vizy, E. K., 2017: The South Atlantic subtropical high: Climatology
580 and interannual variability. Journal of Climate, 30, 3279–3296. https://doi.org/10.1175/JCLI-
581 D-16-0705.1
582 Thomas, N., and Nigam, S., 2018: Twentieth-century climate change over Africa: Seasonal
583 hydroclimate trends and Sahara Desert expansion. Journal of Climate, 31, 3349–3370.
584 https://doi.org/10.1175/JCLI-D-17-0187.1.
585 Thorncroft, C. D., Nguyen, H., Zhang, C., and Peyrille, P., 2011: Annual cycle of the West
586 African monsoon: Regional circulations and associated water vapour transport. Quarterly
587 Journal of the Royal Meteorological Society, 137, 129–147. https://doi.org/10.1002/qj.728.
588 Vizy, E. K., Cook, K. H., Crétat, J., and Neupane, N., 2013: Projections of a wetter sahel in the
589 twenty-first century from global and regional models. Journal of Climate, 26, 4664–4687.
590 https://doi.org/10.1175/JCLI-D-12-00533.1.
591 Vizy, E. K., and Cook, K. H., 2017: Seasonality of the observed amplified Sahara warming
592 trend and implications for Sahel rainfall. Journal of Climate, 30, 3073–3094.
593 https://doi.org/10.1175/JCLI-D-16-0687.1.
594 Wang, S., Sobel, A. H., Zhang, F., Qiang Sun, Y., Yue, Y., and Zhou, L., 2015: Regional
595 simulation of the October and November MJO events observed during the CINDY/DYNAMO
596 field campaign at gray zone resolution. Journal of Climate, 28, 2097–2119.

https://doi.org/10.1175/JCLI-D-14-00294.1.

Wang, Z., Duan, A., Yang, S., and Ullah, K., 2017: Atmospheric moisture budget and its regulation on the variability of summer precipitation over the 27ibetan plateau. Journal of Geophysical Research Atmospheres, 122, 614–630. https://doi.org/10.1002/2016JD025515.

Wei, N., Zhou, L., Dai, Y., Xia, G., and Hua, W., 2017: Observational Evidence for Desert Amplification Using Multiple Satellite Datasets. Scientific Reports, 7, 1–15. https://doi.org/10.1038/s41598-017-02064-w.

Zangvil, A., Portis, D. H., and Lamb, P. J., 2001: Investigation of the large-scale atmospheric moisture field over the midwestern United States in relation to summer precipitation. Part I: Relationships between moisture budget components on different timescales. Journal of Climate, 14, 582–597. https://doi.org/10.1175/1520-0442(2001)014<0582:IOTLSA>2.0.CO;2.

Zangvil, A., Portis, D. H., and Lamb, P. J., 2004: Investigation of the large-scale atmospheric moisture field over the midwestern United States in relation to summer precipitation. Part II: Recycling of local evapotranspiration and association with soil moisture and crop yields. Journal of Climate, 17, 3283–3301. https://doi.org/10.1175/1520-0442(2004)017<3283:IOTLAM>2.0.CO;2.

Zavadoff, B. L., and Kirtman, B. P., 2020: Dynamic and thermodynamic modulators of European atmospheric rivers. Journal of Climate, 33, 4167–4185. https://doi.org/10.1175/JCLI-D-19-0601.1.

Zhou, L., Chen, H., and Dai, Y., 2015: Stronger warming amplification over drier ecoregions observed since 1979. Environmental Research Letters, 10, 64012. https://doi.org/10.1088/1748-9326/10/6/064012.

Zhou, L., 2016: Desert Amplification in a Warming Climate. Scientific Reports, 6, 1–13.

https://doi.org/10.1038/srep31065.

Zhou, L., Chen, H., Hua, W., Dai, Y., and Wei, N., 2016: Mechanisms for stronger warming over drier ecoregions observed since 1979. Climate Dynamics, 47, 2955–2974. https://doi.org/10.1007/s00382-016-3007-9.

Zhou, L., 2021: Diurnal asymmetry of desert amplification and its possible connections to planetary boundary layer height: a case study for the Arabian Peninsula. Climate Dynamics, 56, 3131–3156. https://doi.org/10.1007/s00382-021-05634-x.

Zhou, L., Tian, Y., Wei, N., Ho, S. P., and Li, J., 2021: Rising planetary boundary layer height over the Sahara Desert and arabian peninsula in a warming climate. Journal of Climate, 34, 4043–4068. https://doi.org/10.1175/JCLI-D-20-0645.1.

Zhou, Y., Kim, H., and Waliser, D. E., 2021: Atmospheric River Lifecycle Responses to the Madden-Julian Oscillation. Geophysical Research Letters, 48, 1–10. https://doi.org/10.1029/2020GL090983.

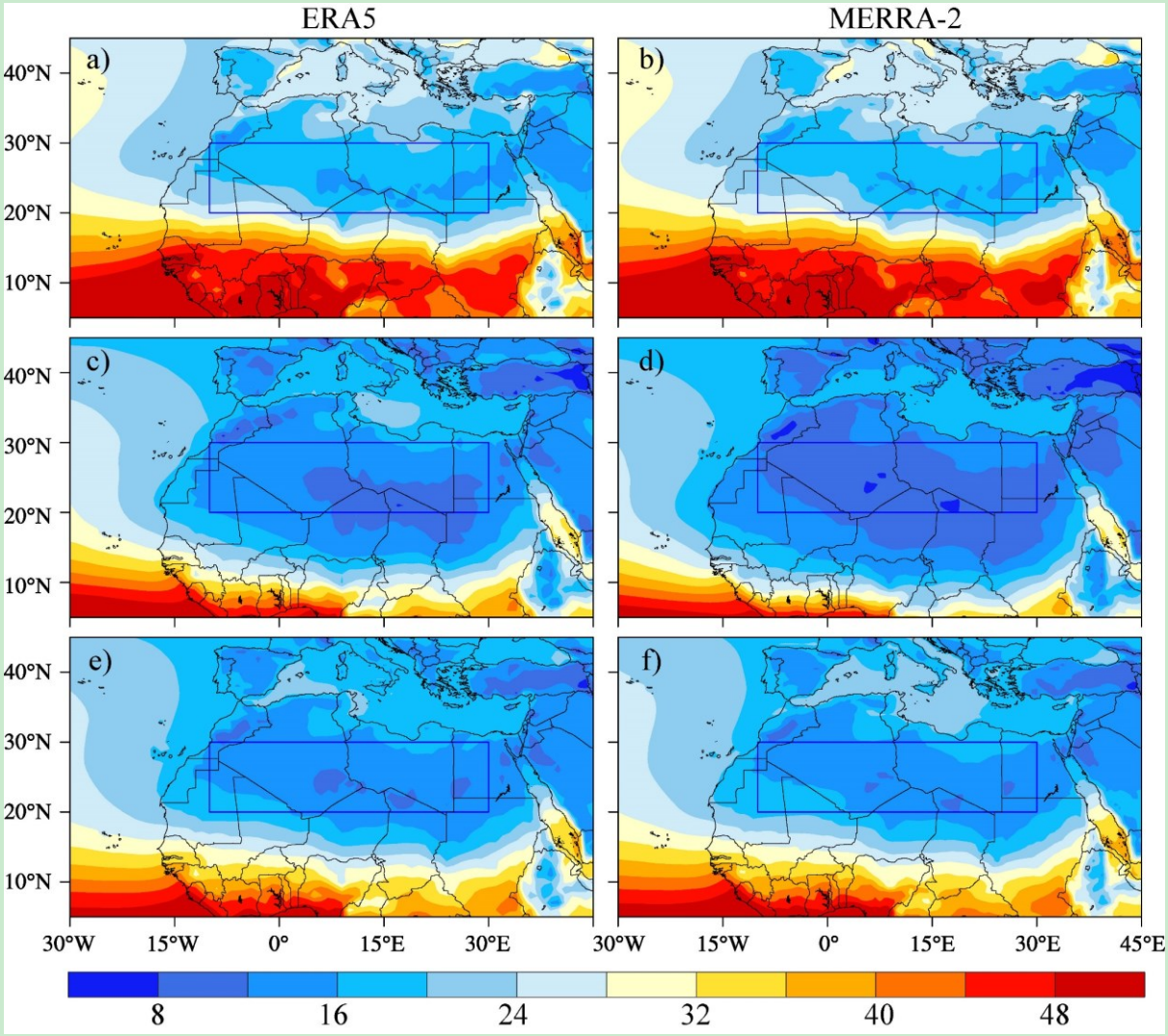

FIGURE 1 Climatological JJA (a, b), DJF (c, d) and annual (e, f) TPW (kg m^{-2}) for ERA5 (left) and MERRA-2 (right). The rectangle boxes in blue (20°N to 30°N and 10°W to 30°E) represents the boundaries of the Sahara Desert.

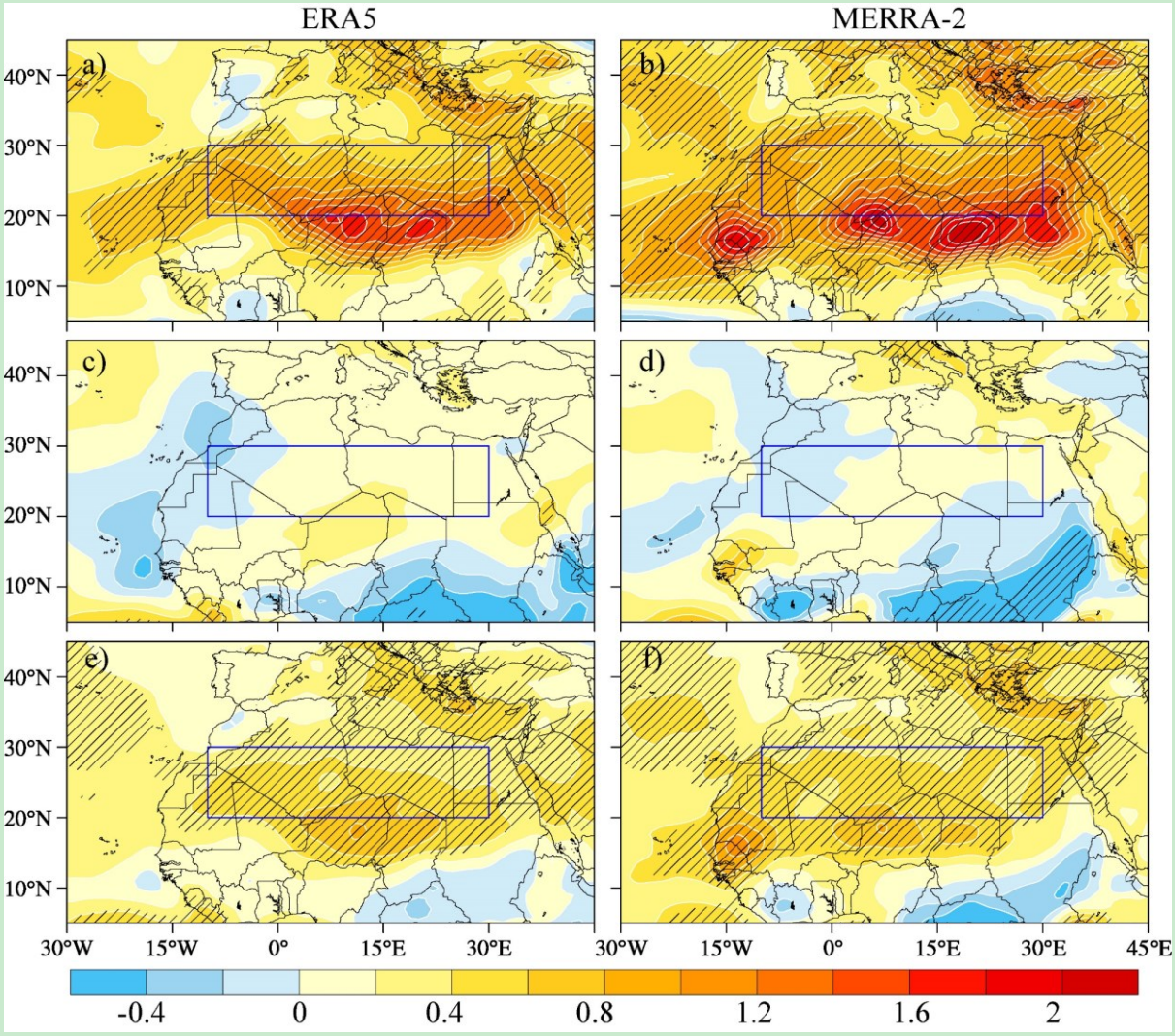

FIGURE 2 JJA (a, b), DJF (c, d) and annual (e, f) trends of TPW (kg m^{-2} $decade^{-1}$) for ERA5 (left) and MERRA-2 (right). The area slashed denotes the region with significance of TPW trends at the 99% level of confidence. The rectangle boxes in blue (20°N to 30°N and 10°W to 30°E) represents the boundaries of the Sahara Desert.

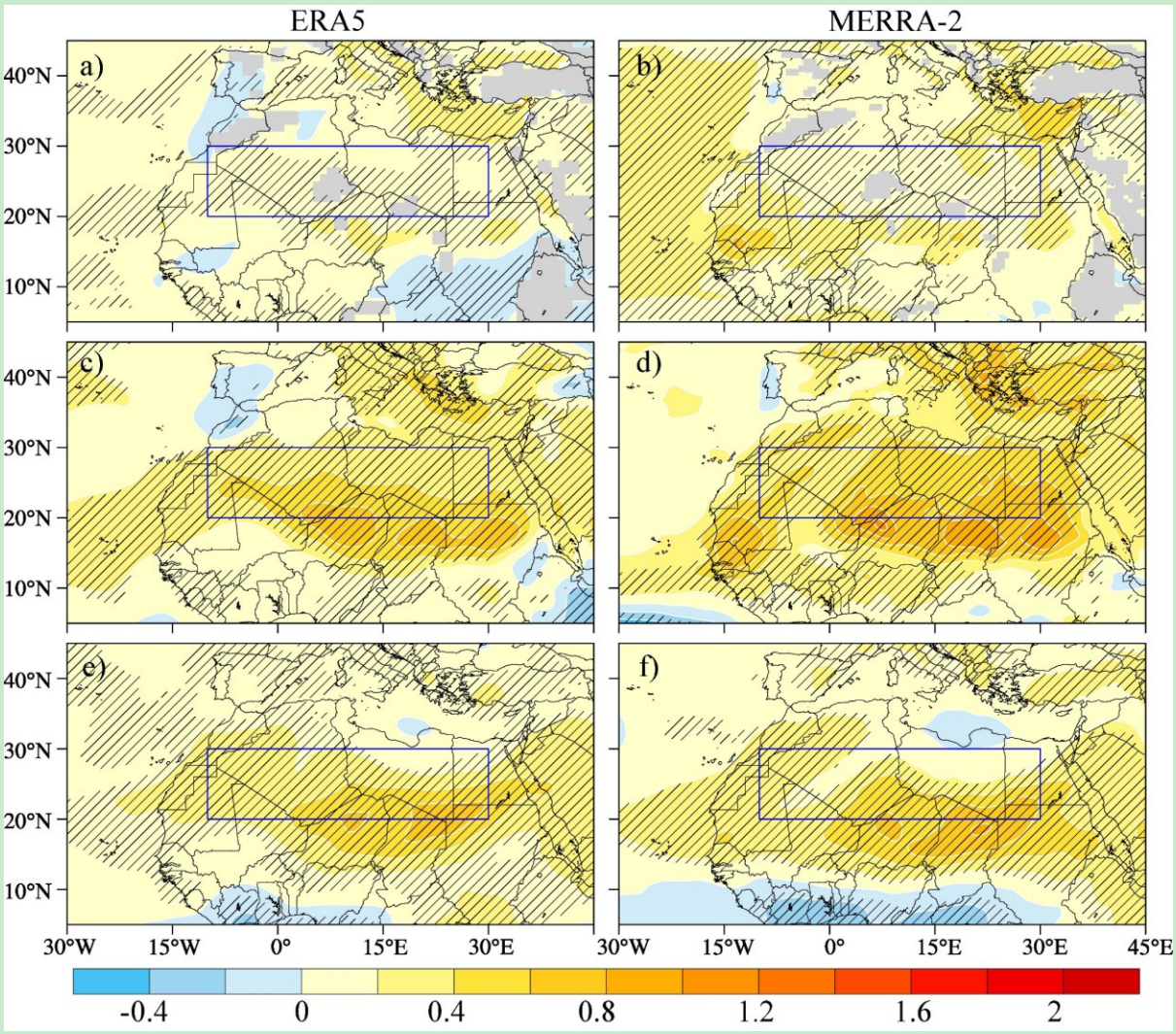

FIGURE 3 JJA trends of TPW (kg m^{-2} $decade^{-1}$) from the surface to 900 hPa (a, b), 900-700 hPa (c, d) and 700-500 hPa (e, f) for ERA5 (left) and MERRA-2 (right). The area slashed denotes the region with significant TPW trends at the 90% level of confidence. The rectangle boxes in blue (20°N to 30°N and 10°W to 30°E) represents the boundaries of the Sahara Desert.

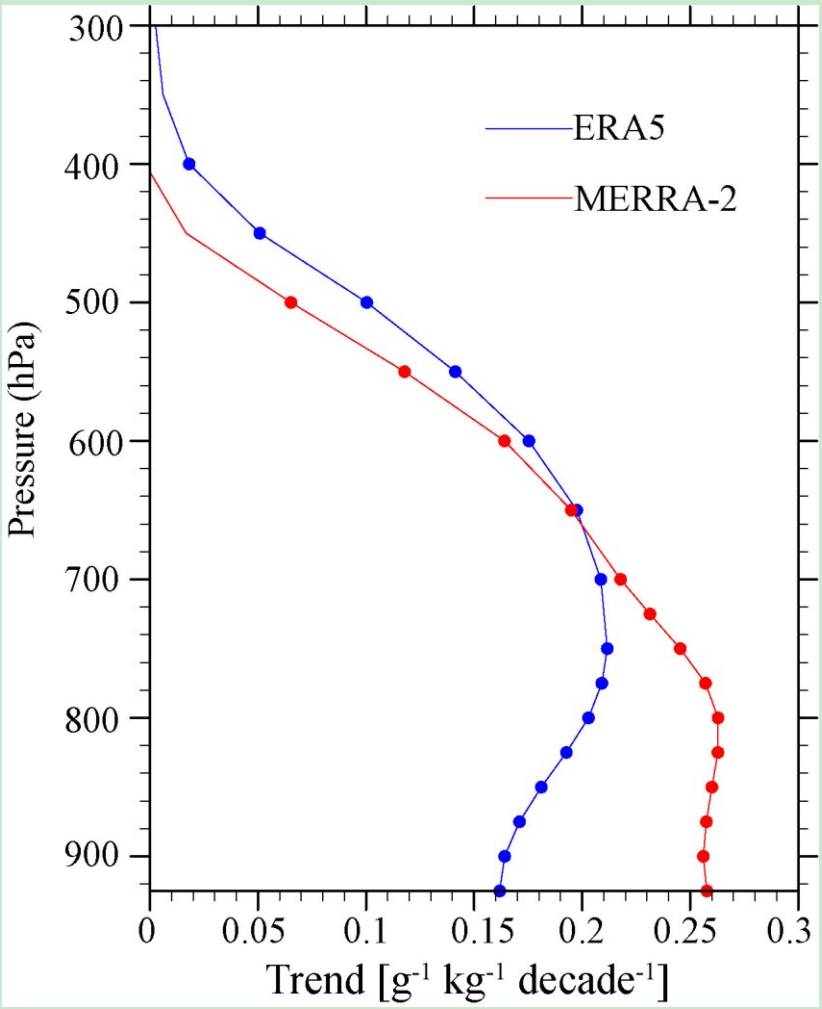

FIGURE 4 The vertical profile of the area average JJA *q* trend (g^{-1} kg^{-1} $decade^{-1}$) over the Sahara Desert. The dots denote significance of *q* trends at the 99% level of confidence.

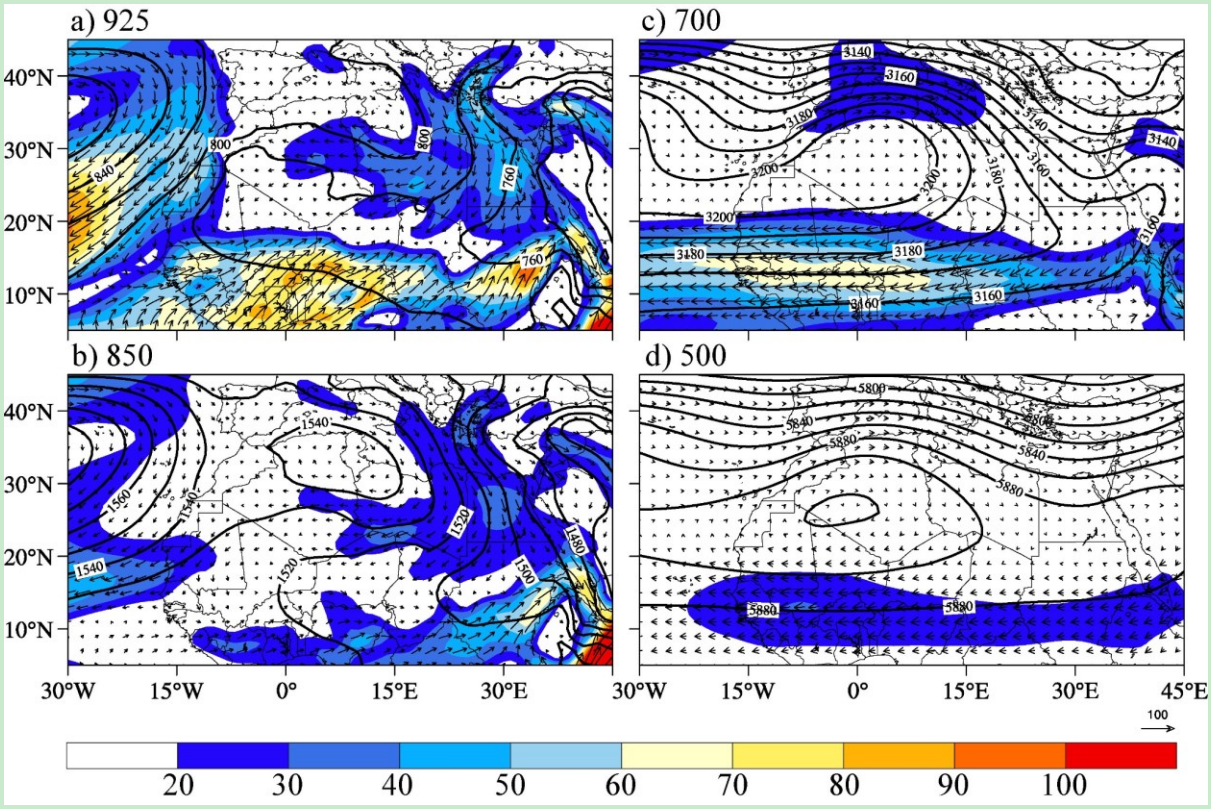

FIGURE 5 Climatological moisture transport $q\vec{V}$ (vectors; (g/kg)*(m/s)), its magnitude (shading), and geopotential height (black contours; m) for 925 hPa (a), 850 hPa (b), 700 hPa (c) and 500 hPa (d) over JJA from 1981-2020 for ERA5.

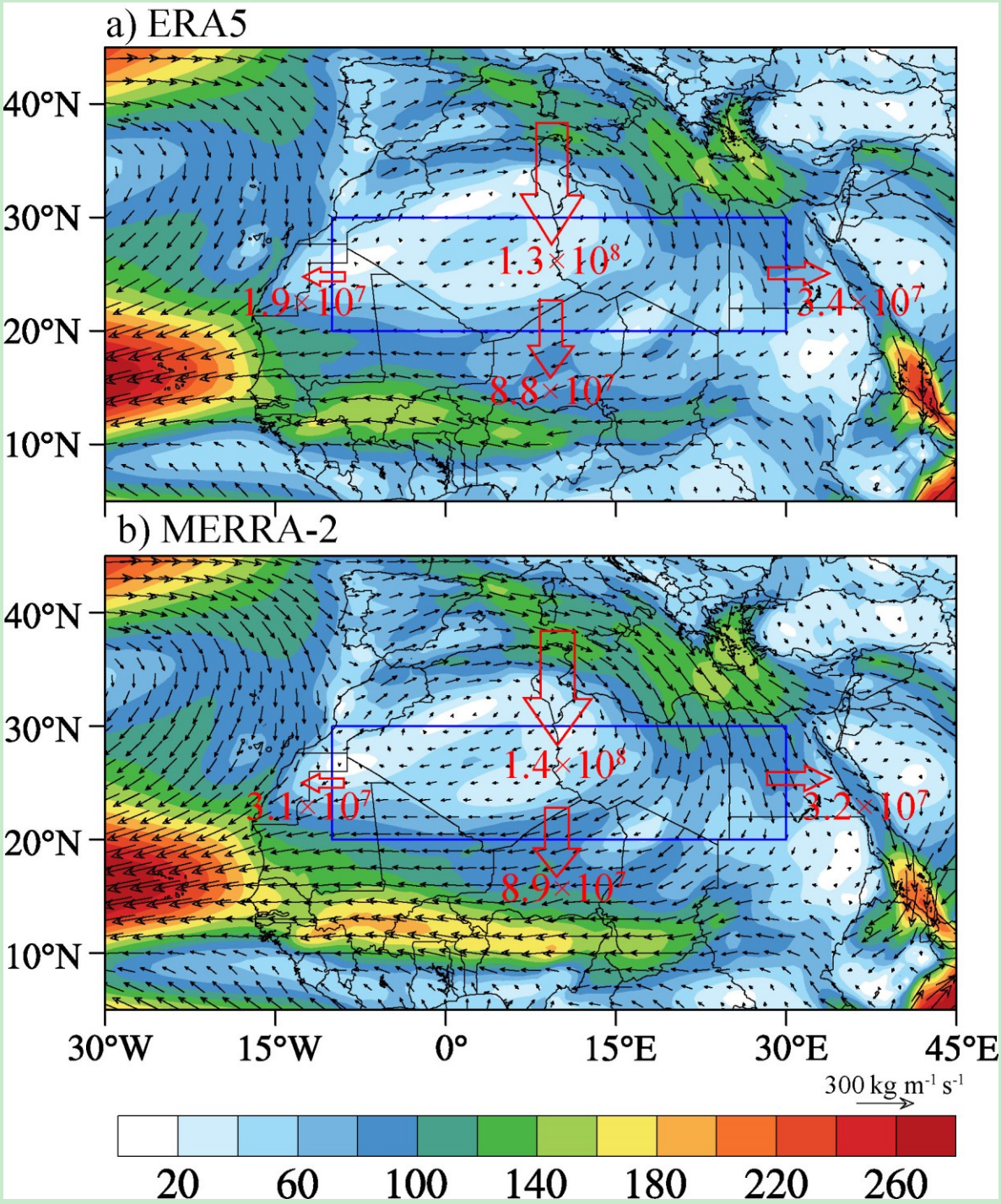

721

722 **FIGURE 6** Climatology of IVT (vectors; kg m^{-1} s^{-1}) and its magnitude (shading) in summer for ERA5 (a)
723 and MERRA-2 (b) from 1981-2020. The arrows and values represent the direction and magnitude of
724 moisture flux for each boundary (kg s^{-1}).
725
726
727
728
729
730
731
732

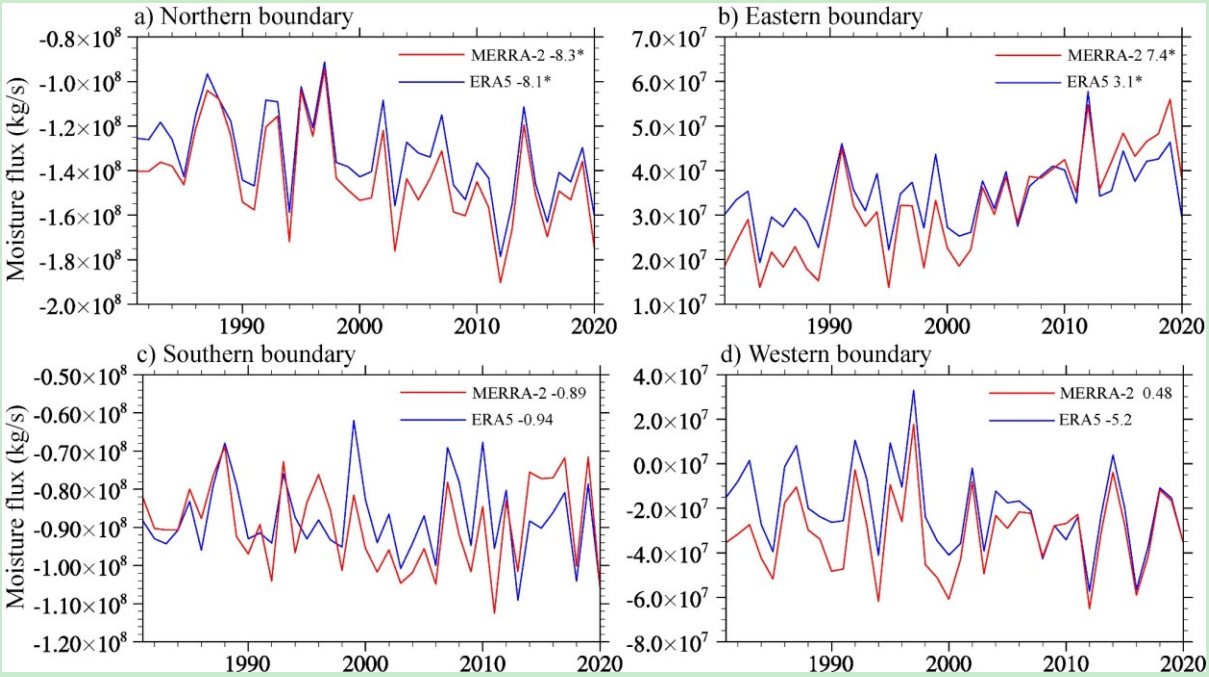

FIGURE 7 Interannual variation of summer moisture fluxes across (a) Northern, (b) Eastern, (c) Southern and (d) Western boundary from ERA5 (blue) and MERRA-2 (red). The associated numbers in the figure legend denote the trends (10^6 kg s^{-1} $decade^{-1}$). Trends statistically significant at the 99% level of confidence are labeled with '*'.

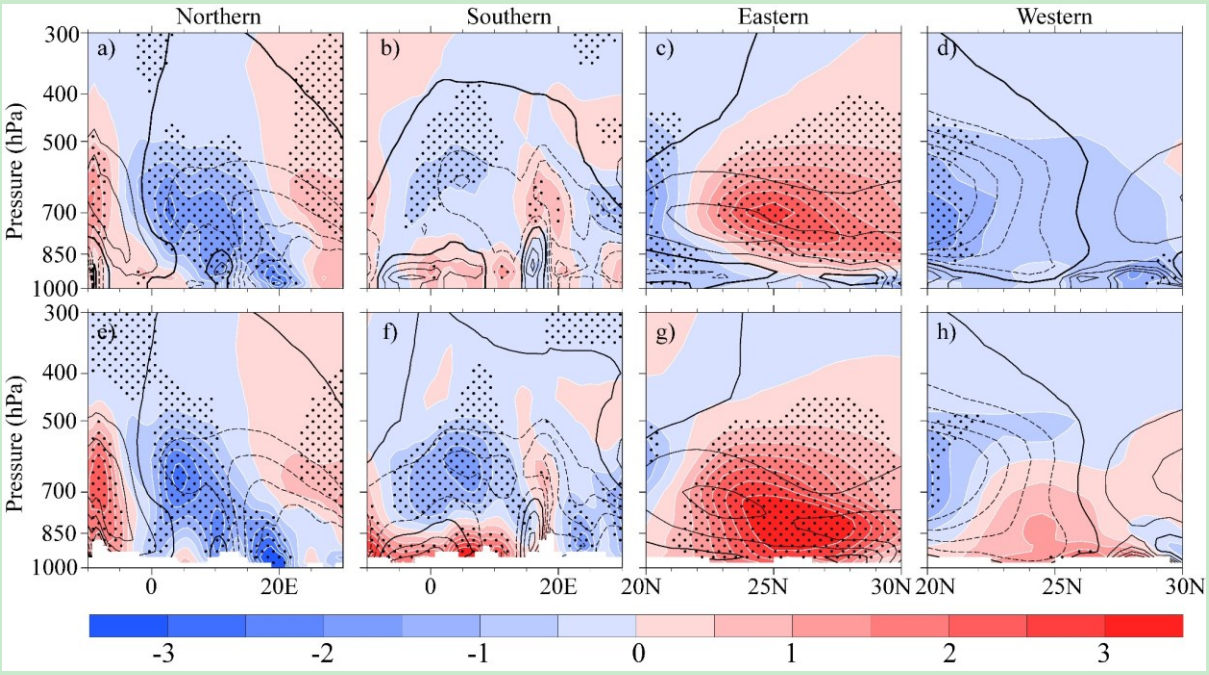

FIGURE 8 Vertical cross section of the trends of moisture transport (shading; (g/kg)*(m/s)*decade^{-1}) and climatology moisture transport (blank contours; positive values denoted by solid lines and negative values denoted by dashed lines; (g/kg)*(m/s)) for the Northern (a, e), Southern (b, f), Eastern (c, g) and Western (d, h) boundary from ERA5 (a-d) and MERRA-2 (e-h). In the Northern (a, e) and Southern (b, f) boundaries, solid (positive) lines represent southerly moisture flux. In the Eastern (c, g) and Western (d, h) boundaries, solid (positive) lines represent westerly moisture flux. Stippling denotes significance of the moisture flux trends at the 95% level of confidence.

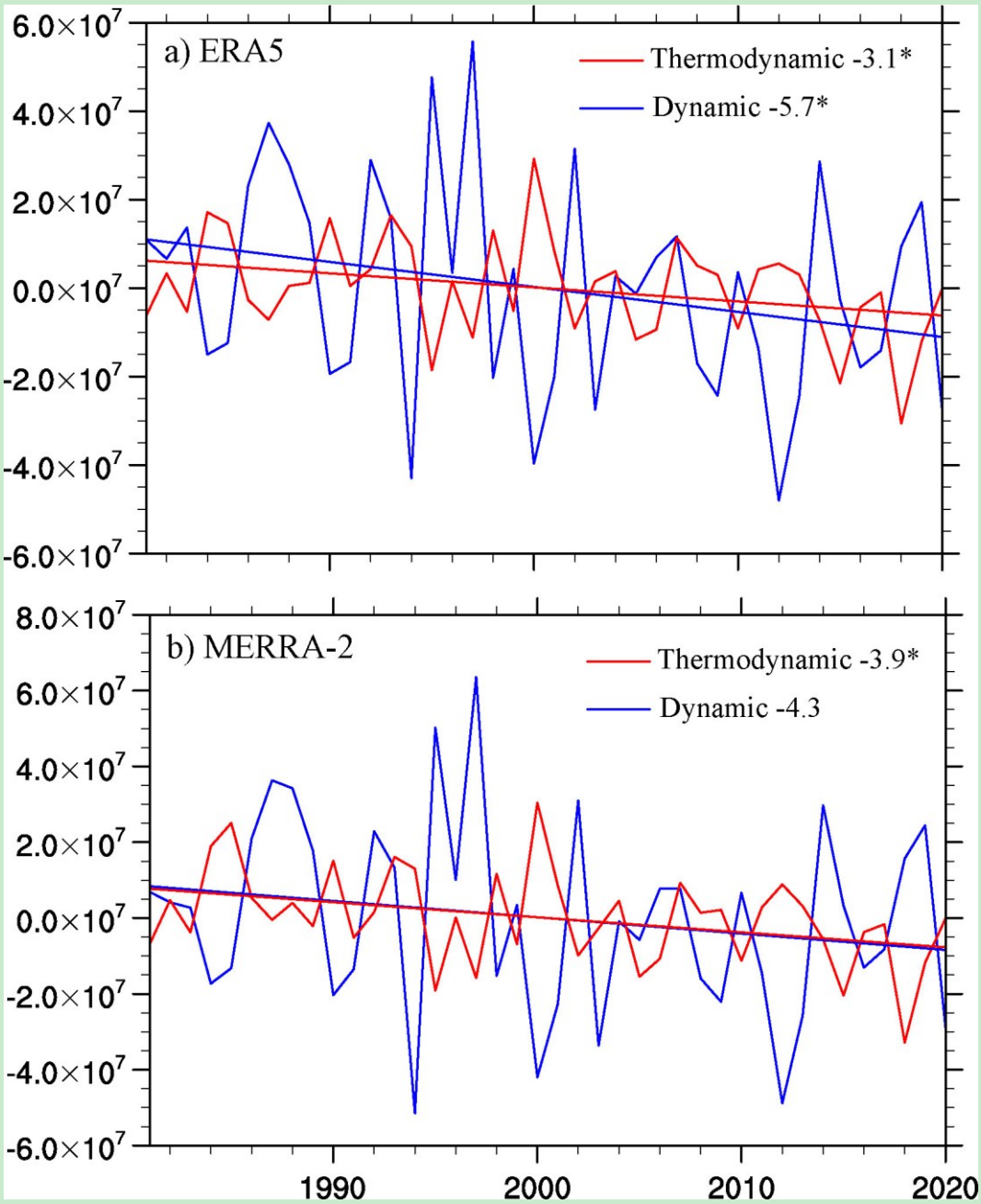

FIGURE 9 Interannual variation of the moisture flux at the northern boundary caused by dynamic (blue) and thermodynamic term (red) from (a) ERA5 and (b) MERRA-2. The associated numbers in the figure legend denote the trends (10^6 kg s^{-1} $decade^{-1}$). Trends statistically significant at the 90% level of confidence are labeled with '*'.

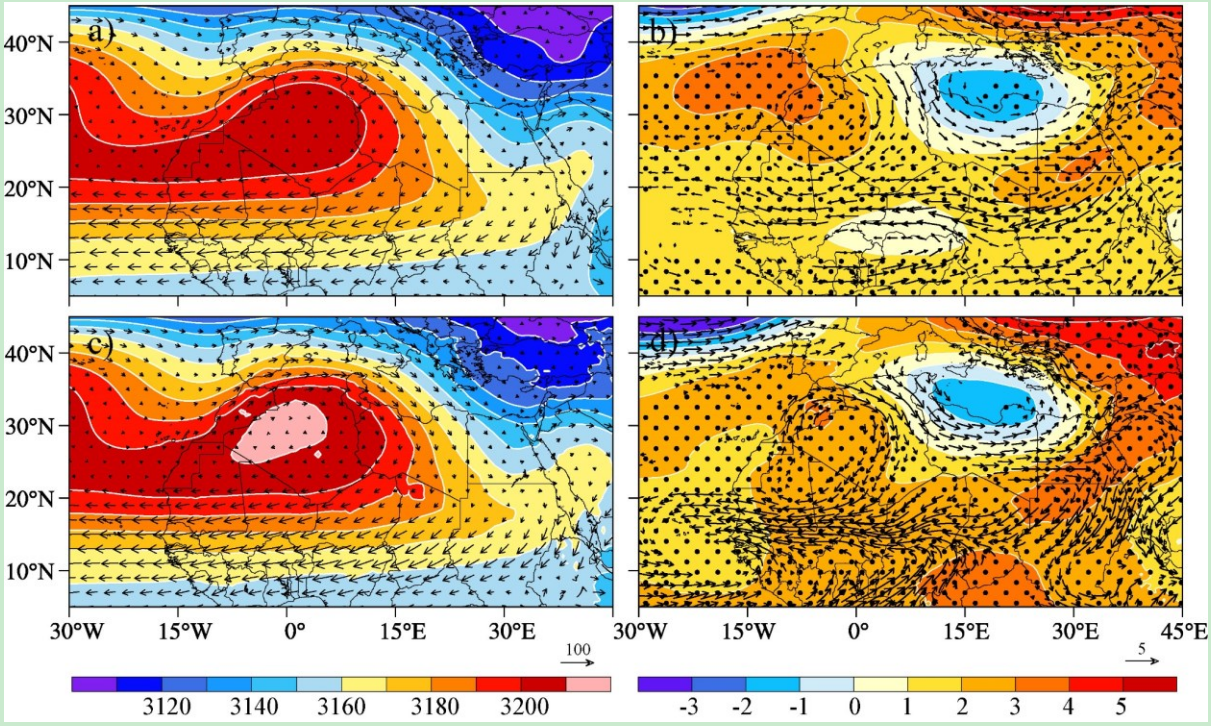

FIGURE 10 700 hPa summer climatological geopotential heights (shading; m) and moisture transport (vectors; (g/kg)*(m/s)) for (a) ERA5, (c) MERRA-2. Also shown are the 700 hPa summer geopotential heights trend (shading; m decade^{-1}) and moisture transport trend (vectors; (g/kg)*(m/s)*decade^{-1}) significant at 90% level of confidence for (b) ERA5, (d) MERRA-2. Stippling denotes significance of geopotential heights trends at the 95% level of confidence.

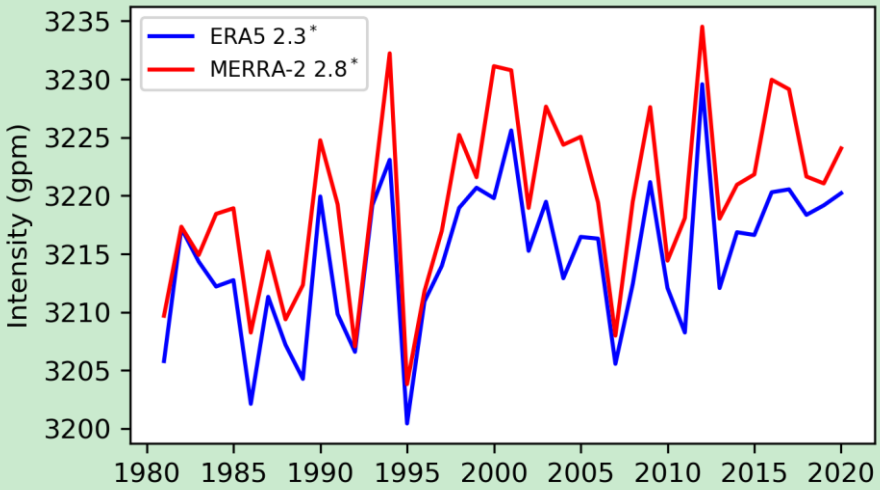

FIGURE 11 Interannual variation of the Saharan High intensity for ERA5 (blue) and MERRA-2 (red). The associated numbers in the figure legend denote the trends (gpm decade^{-1}). Trends statistically significant at the 95% level of confidence are labeled with '*'.

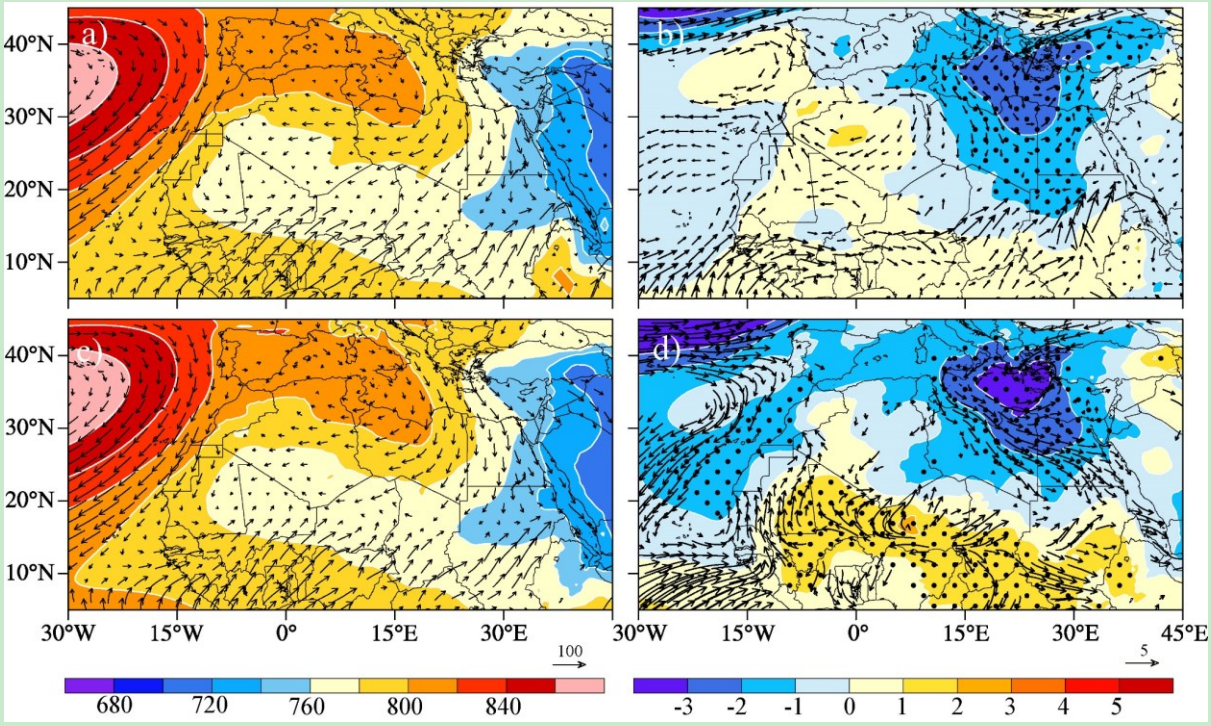

FIGURE 12 As in Figure 10 but for 925 hPa.

866 **TABLE 1** Climatological water vapor budget values (mm day^{-1}) and trends (mm day^{-1} decade^{-1}; in
867 parentheses) for ERA5 (column 2) and MERRA-2 (column 3). Statistically significant values at the 99%
868 confidence level are italicized and boldfaced.

	ERA5	MERRA-2
F_{north}	2.31 (***0.141***)	2.49 (***0.145***)
F_{south}	-1.54 (-0.016)	-1.56 (-0.0155)
F_{east}	-0.6 (***-0.055***)	-0.56 (***-0.129***)
F_{west}	-0.35 (-0.091)	-0.55 (-0.008)
E	0.093 (***0.004***)	0.08 (0.002)
P	0.032 (***0.006***)	0.036 (***0.01***)
R	0.09 (0.008)	0.14 (0.005)

869